Eurographics / IEEE Symposium on Visualization 2011 (EuroVis 2011)
H. Hauser, H. Pfister, and J. J. van Wijk
(Guest Editors)

Volume 30 (2011), Number 3

Visualizing the Positional and Geometrical Variability of Isosurfaces in Uncertain Scalar Fields

Tobias Pfaffelmoser, Matthias Reitinger and Rüdiger Westermann

Computer Graphics and Visualization Group, Technische Universität München, Germany

Abstract

We present a novel approach for visualizing the positional and geometrical variability of isosurfaces in uncertain 3D scalar fields. Our approach extends recent work by Pöthkow and Hege [PH10] in that it accounts for correlations in the data to determine more reliable isosurface crossing probabilities. We introduce an incremental update-scheme that allows integrating the probability computation into front-to-back volume ray-casting efficiently. Our method accounts for homogeneous and anisotropic correlations, and it determines for each sampling interval along a ray the probability of crossing an isosurface for the first time. To visualize the positional and geometrical uncertainty even under viewing directions parallel to the surface normal, we propose a new color mapping scheme based on the approximate spatial deviation of possible surface points from the mean surface. The additional use of saturation enables to distinguish between areas of high and low statistical dependence. Experimental results confirm the effectiveness of our approach for the visualization of uncertainty related to position and shape of convex and concave isosurface structures.

Categories and Subject Descriptors (according to ACM CCS): I.3.3 [Computer Graphics]: Picture/Image Generation—Display algorithms, Viewing algorithms

1. Introduction

Numerical data that is produced by measurements or numerical simulations is always affected by uncertainties due to errors in the acquisition process, the underlying physical model, or the used computational method. One has to be aware that the information contained in this data is never exact, and that analyzing the data while ignoring local or global uncertainties can result in misclassifications, misinterpretations, and false assumptions. This uncertainty cannot be eliminated, but it can be provided to the user as possible variations of relevant features.

Although uncertainty visualization is regarded one of the grand challenges in visual data exploration [Joh04], it is fair to say that standardized procedures for modeling and visualizing the effect of uncertainty on features in multidimensional data are rare. The most recent approach by Pöthkow and Hege [PH10] suggests to model the uncertainty stochastically, and to derive probability distributions for particular events that correspond to relevant features, e.g., the crossing of isosurfaces in volume ray-casting. This allows quantifying the spatial distribution of uncertain features, enabling a statistical analysis of the effect of uncertainties in the input data on the uncertainty of these features.

Inspired by [PH10], the motivation behind our work is twofold: Firstly, we are aiming for the integration of data correlations into the stochastic uncertainty model to enable a more reliable computation of isosurface crossing probabilities along the view rays. When ignoring sample correlations, a zero correlation between very close samples is assumed. This contradicts the assumption of local data continuity and results in vastly overestimated probabilities. This effect is demonstrated in Figure 1, where the uncertainty is modeled as a multi-dimensional Gaussian random function. Since its density function depends on pair-wise sample correlations, the probabilities of crossing a surface along the view rays under the assumption of distance-based correlation (a) are significantly different to the probabilities when constant correlation is assumed (b).

Our second goal is to develop new strategies for mapping uncertainty to optical properties in a way that allows visualizing the positional and geometrical variability independently of the viewing direction. In this way we are ad-

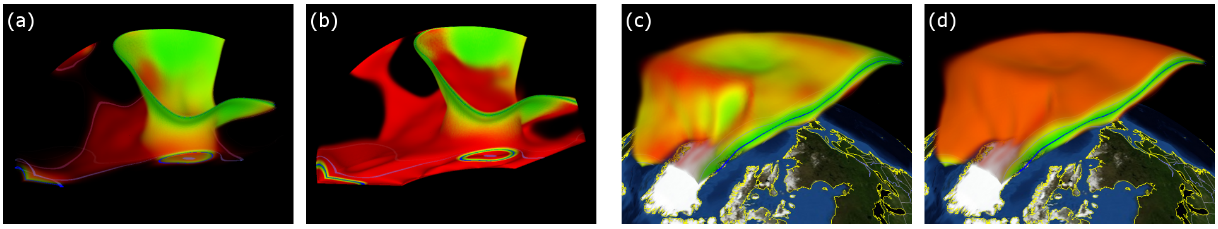

Figure 1: *Volume visualization of isosurface crossing probabilities in uncertain 3D scalar fields (absorption is proportional to probability, distance to mean-surface is color-coded from green (low) to red (high)). (a) Our approach with sample correlations incorporated. (b) Probabilities are vastly overestimated when correlations are not considered. (c) Our approach supports view-independent uncertainty perception by using color to indicate spatial distance. (d) Color mapping based on stochastic distance.*

dressing the problem that positional uncertainties of isosurfaces can often be revealed only in 2D cross-sections or if the viewer is *not* looking along the surface normal direction. If the isosurface position varies along this direction, it can be perceived clearly only when viewing is orthogonal to the normal. To overcome this limitation we propose an Euclidean distance measure that assigns to each possible isosurface position the spatial deviation from the mean surface. This measure is used in a novel color mapping scheme to assess the uncertainty that is related to the shape of an isosurface even under viewing directions parallel to the surface normal. In Figure 1, the effect of this visual encoding (c) is compared to an encoding that only considers the deviation in probability space (d).

The remainder of this paper is as follows: In the next section we review previous work that is related to ours. Then we briefly describe the basic concepts underlying the stochastic modeling of uncertainty that is used in our work. In section 4 we present a novel algorithm for estimating the positional probability density of the isosurface occurrence in a 3D uncertain scalar field along view rays. A new approach for visualizing the variability of isosurfaces by taking into account their deviation from a mean surface is proposed in 5. Different mappings of the isosurface variability to optical properties are discussed in section 6. Results and an assessment of the practical relevance of the proposed uncertainty visualization techniques is given in section 7. In section 8 we provide implementation details, and we conclude the paper with some ideas on future challenges in the field.

2. Related Work

In scientific visualization, the indication of accuracy in the displayed results has been mainly restricted to particular domains such as geographical information systems [MRH*05], seismology [BAF08] and astrophysics [LFLH07]. For an overview and taxonomy of uncertainty visualization let us refer to [JS03, THM*05, GS06]. [SZD*10] pursued a case study to analyze the effectiveness of uncertainty visualization techniques for 1D and 2D datasets.

Major efforts have been put on the visualization of the variability of isosurfaces in uncertain scalar fields. [PWL97, JS03] proposed to augment a mean surface by additional surfaces that enclose areas of high confidence. The use of opacity to show spatial contiguity and isosurface confidence regions was demonstrated in [ZWK10]. Flowlines were introduced in [KWTM03] to visualize the uncertainty of material boundaries. In [GR04] an isosurface was modeled as a point set, and points were displaced from their original position by an amount proportional to the local uncertainty. The animation of possible isosurface positions over time was demonstrated in [Bro04]. [RLBS03] indicate data uncertainty by mapping color and texture on isosurfaces. Recently, [PH10] presented a method for visualizing the positional variability around a mean isosurface using direct volume rendering. Based on probability theory, they introduced mathematical formulations for the positional uncertainty of isosurfaces and employed the concept of numerical condition for visually presenting how errors in the input data are amplified in isosurface extraction.

The visualization of uncertainty as a secondary data source using icons and glyphs has been considered in [WPL02, SZD*10]. [LLPY07] applied animations to vary the appearance for uncertain regions in medical datasets. In [DKLP02], opacity deviations and noise effects were used to provide qualitative measures for the uncertainty in volume rendering. [OGHT10] extended the concept of vector field topology to uncertain vector fields by introducing density distribution functions. Uncertainty in classification and segmentation was addressed in [KVUS*05].

3. Stochastic Modeling of Uncertainties

In the context of 3D scalar datasets, by uncertainty we understand the mean deviation of the data samples from a true or assumed value without precise knowledge of the magnitudes of these deviations. We assume the data samples to be attributed by parameterized uncertainty, which will be considered in the visualization of the positional and geometrical variability of isosurfaces in the data.

3.1. Uncertainty Representation

The 3D scalar field is assumed a discrete sampling of a mapping from the continuous spatial domain $\mathbb{S} \subseteq \mathbb{R}^3$ into $\mathbb{R}$. The sampling is represented by a finite set of n *spatial points* $\mathbb{S}_n = \{\mathbf{x}_i : \mathbf{x}_i \in \mathbb{S}, i \in \{1,2,...,n\}\} \subset \mathbb{S}$. The mapping and its uncertainty is modeled as a *random function* $Y : \mathbb{S}_n \to \mathbb{R}, \mathbf{x} \mapsto Y(\mathbf{x})$, where for each spatial point $\mathbf{x}_i$ the mapping $Y(\mathbf{x}_i)$ is considered a *random variable*.

The random function is characterized by a n-dimensional probability density function $f(y_1, y_2, ..., y_n)$, where y_i is a *realization* or *observed value* of the random variable $Y_i := Y(\mathbf{x}_i)$. Throughout this work, f is assumed a multivariate *normal* probability density function (MNPDF). MNPDFs are commonly used for modeling probability densities since they have often shown to adequately represent random fluctuations in measured values of deterministic quantities. In order to fully characterize f, for every sample point the mean value $\mu_i := \mu(Y_i)$ and the standard deviation $\sigma_i := \sigma(Y_i)$ have to be known, and pair-wise correlations $\rho_{ij} := \rho(Y_i, Y_j)$ are required to build the covariance matrix of a MNPDF.

3.2. Correlation

There are many ways to understand the meaning and effect of correlation [RN88]. We will interpret it as a measure for *stochastic dependence* and as a modeling tool for smoothness and continuity. For MNPDFs, correlation is specified in the form of a symmetric correlation matrix, which contains *correlation coefficients* $-1 \leq \rho(Y_i, Y_j) \leq 1$ between two components of the multidimensional random function Y. These coefficients are a direct measure of the stochastic dependence of two components of Y. If Y_i deviates positively from μ_i by the magnitude $\Delta\mu$, a large correlation value indicates that Y_j also deviates positively ($\rho_{ij} \approx 1$) or negatively ($\rho_{ij} \approx -1$) around $\Delta\mu \cdot \frac{\sigma_j}{\sigma_i}$ from μ_j. For $\rho_{ij} \approx 0$ the realizations of Y_j are considered uncorrelated from Y_i.

Discrete samplings of a continuous mapping usually assume a certain local smoothness and at least local continuity of the sampled quantity. To achieve this, random function correlation is described by *spatial distance dependent correlation functions* [Tar05]. In the case of a MNPDF one typically uses the *exponential correlation function* (ECF)

$$\rho(Y_i, Y_j) = \exp(-\tau \|\mathbf{x}_i - \mathbf{x}_j\|) \ \ , \ \ \mathbf{x}_i, \mathbf{x}_j \in \mathbb{S}_n, \qquad (1)$$

which assigns higher correlations to random variables of points with smaller Euclidean distance. If the correlation strength τ is defined locally for each point in $\mathbb{S}_n$, the ECF becomes

$$\rho(Y_i, Y_j) = \exp(-0.5(\tau(\mathbf{x}_i) + \tau(\mathbf{x}_j)) \|\mathbf{x}_i - \mathbf{x}_j\|). \qquad (2)$$

To model anisotropic correlations, the parameter τ can be made dependent on a specific direction. For a unit vector $\mathbf{r}$, the parameter τ at point $\mathbf{x}_i$ in direction $\mathbf{r}$ is then given by $\tau(\mathbf{x}_i, \mathbf{r}) = \mathbf{r}^T \mathbf{T}(\mathbf{x}_i)\mathbf{r}$, where $\mathbf{T}$ is a rank-2 tensor that models the anisotropy. This tensor can either be derived from the correlations in the data samples, or it can be specified based on a priori knowledge. If one assumes at every point $\mathbf{x}_i$ different parameters $\tau_1(\mathbf{x}_i)$, $\tau_2(\mathbf{x}_i)$, and $\tau_3(\mathbf{x}_i)$ along the three major spatial directions, the tensor coefficients are given as $T_{kl} = 0$ for $k \neq l$ and $T_{kk} = \tau_k$. The parameters τ_k can be computed by solving the linear equation system

$$\tau_1(\mathbf{x}_i)(x_{h1} - x_{i1})^2 + \tau_2(x_i)(x_{h2} - x_{i2})^2 + \tau_3(x_i)(x_{h3} - x_{i3})^2 = \\ = -\log(|\rho(Y_i, Y_h)|) \|\mathbf{x}_h - \mathbf{x}_i\| \ \ , \ \ h \in \{k, l, m\} \qquad (3)$$

for at least three neighboring points $\mathbf{x}_k$, $\mathbf{x}_l$, and $\mathbf{x}_m$ of $\mathbf{x}_i$ and correlation values $\rho(Y_i, Y_k)$, $\rho(Y_i, Y_l)$ and $\rho(Y_i, Y_m)$ usually given by the data as correlation matrix. In this formulation, x_{is} denotes the s-th component of vector $\mathbf{x}_i$. For a homogeneous correlation model, $\tau(\mathbf{x}_i)$ can be defined as the mean of $\tau_1(\mathbf{x}_i)$, $\tau_2(\mathbf{x}_i)$, and $\tau_3(\mathbf{x}_i)$. Note, that only the magnitude of the local correlation is modeled by the ECF. The sign can be stored as binary value for each spatial direction at point $\mathbf{x}_i$.

3.3. Stochastic Distance Function

To relate the possible occurrence of an isosurface to the local uncertainty, the *stochastic distance function* (SDF)

$$\Psi_\theta(\mathbf{x}_i) := \frac{\mu_i - \theta}{\max(\sigma_i, \sigma_{min})} \quad \mathbf{x}_i \in \mathbb{S}_n, \theta \in \mathbb{R}, \qquad (4)$$

is often used. Here, θ refers to a specified isovalue, and a minimum standard deviation σ_{min} is assumed to avoid numerical problems.

The SDF corresponds to the 1-dimensional formulation of the Mahalanobis distance [Mah36, DMJRM00], and it indicates at point $\mathbf{x}_i$ the distance of the mean value μ_i to the isovalue in number of σ_i. SDF fields are often used to depict the confidence volume containing the level-θ isosurface with a certain probability [ZWK10], or the SDF values are used for color coding uncertain isosurfaces as in [PH10]. Our algorithm computes the SDF for all grid vertices on-the-fly and uses these values either for computing isosurface crossing probabilities as discussed in section 4 or for determining probability gradients as described in section 5.

4. Probabilistic Isosurface Extraction

We now describe our approach for computing positional probabilities of isosurfaces in uncertain 3D scalar fields via volume ray-casting. We assume a 3D grid structure, attributed by a mean μ_i and a standard deviation σ_i at every grid vertex $\mathbf{x}_i$. For a given isovalue this allows computing per-vertex SDF values as described in 3.3. In addition, for every cell a rank-2 tensor is stored according to the ECF model as discussed in 3.2. The 6 distinct tensor values are stored as per-cell attributes. The grid is supposed to be equipped with a local cell-wise interpolation scheme to reconstruct SDF values at any point in the 3D domain.

Isosurface ray-casing is performed by sampling the scalar field along the view rays in front-to-back order. Our approach for uncertainty visualization computes along each ray and in each sampling interval the probability of crossing the isosurface *for the first time*. The technique is intertwined with the front-to-back traversal in that it provides an incremental update-scheme for determining these probabilities solely based on local evaluations.

4.1. Isosurface Crossing Probability

The volume is sampled along each ray at equidistant discrete linear ordered sample points $\{\mathbf{s}_1, \mathbf{s}_2, ..., \mathbf{s}_n\} \subset \mathbb{S}$. At each point $\mathbf{s}_i$ a SDF value ψ_i is obtained via interpolation, and for two consecutive sample points $\mathbf{s}_i$ and $\mathbf{s}_{i+1}$ a correlation value $\rho_i := \rho(Y(\mathbf{s}_i), Y(\mathbf{s}_{i+1}))$ is computed as described in 3.2. From this data the probability p_i for crossing the isosurface in the sampling interval $I_i = [\mathbf{s}_i, \mathbf{s}_{i+1}]$ is calculated.

Notably the probability p_i *cannot* be computed by only considering the current interval. In this case, the probability $p_i + p_{i+1}$ also considers the event of crossing the surface in I_i *and* I_{i+1}. However, to guarantee a reliable positional probability estimation, the event of crossing the isosurface *either* in I_i *or* in I_{i+1} has to be considered, i.e., based on a XOR combination of disjoint crossing events. Therefore, we introduce the events

$$Y_i^+ := (Y(\mathbf{s}_i) \geq \theta) \tag{5}$$

$$Y_i^- := (Y(\mathbf{s}_i) < \theta), \tag{6}$$

which compare the value of the random variable Y at the sample points to the isovalue. By using these events, the *positive first crossing event*

$$C_i^+ := Y_1^- \cap Y_2^- \cap ... \cap Y_i^- \cap Y_{i+1}^+ \tag{7}$$

can be defined; it describes the incident that the isosurface is crossed (from lower to higher values) in interval I_i *for the first time*. The negative crossing event C_i^- is defined respectively. For simplicity, in the following we will only investigate C^+ — all results apply in the same way for C^-.

The proposed event formulation guarantees that C_i^+ and C_j^+ for $i \neq j$ are disjoint events that cannot be both true at the same time, i.e., XOR combinations of crossing events are considered. With a probability measure P, the total positive isosurface crossing probability along a ray can then be computed as $\sum P(C_i^+)$. $P(C_i^+)$, and respectively $P(C_i^-)$, provide an indication of the positional variability around the most likely position of the isosurface. In our algorithm we set $p_i := P(C_i^+) + P(C_i^-)$ to account for positive and negative first crossing events. Here we exploit the fact that C_i^+ and C_i^- are also disjoint events.

For computing $P(C_i^+) = P(Y(\mathbf{s}_1) < \theta, Y(\mathbf{s}_2) < \theta, ..., Y(\mathbf{s}_i) < \theta, Y(\mathbf{s}_{i+1}) \geq \theta)$ efficiently, we employ the fact that the probability density function f is assumed to be of MNPDF type (cf. 3.1). In general, one can evaluate the multivariate normal cumulative distribution function (MNCDF) of dimension $i+1$ for each interval I_i. Since this is by far too costly, we propose an efficient method for incrementally updating $P(C_i^+)$ with a minimum of additional operations per interval. Furthermore, we will show that it is possible to compute $P(C_i^+)$ using at most 2-dimensional MNCDFs and, thus, to avoid costly evaluations of high-dimensional MNCDFs.

By using the theory of conditional probability, we can rewrite $P(C_i^+)$ in the following way:

$$P(C_i^+) = P(Y_1^- \cap Y_{i+1}^+ | Y_2^- \cap ... \cap Y_i^-) P(Y_2^- \cap ... \cap Y_i^-) \tag{8}$$

We also know that for a MNPDF with the special requirement $\rho(A,C) = \rho(A,B)\rho(B,C)$ on the correlation coefficients the following rule applies:

$$P(A \cap C | B) = P(A|B)\, P(C|B) \tag{9}$$

Since we use an ECF (cf. 3.2) for the modeling of correlations, pair-wise correlations can be written as

$$\rho(Y(\mathbf{s}_i), Y(\mathbf{s}_{i+m})) = \prod_{j=i}^{i+m-1} \rho(Y(\mathbf{s}_j), Y(\mathbf{s}_{j+1})). \tag{10}$$

This means that the aforementioned requirement is met and (9) can be applied several times to (8) to arrive at the following equation for $P(C_i^+)$:

$$P(C_i^+) = P(Y_1^-) \frac{P(Y_i^- \cap Y_{i+1}^+)}{P(Y_i^-)} \prod_{j=1}^{i-1} \frac{P(Y_j^- \cap Y_{j+1}^-)}{P(Y_j^-)} \tag{11}$$

The high-dimensional MNCDF value $P(C_i^+)$ can be expressed solely by 1- and 2-dimensional MNCDFs of random variables of *consecutive* sample points. Thus, $P(C_i^+)$ can be computed incrementally by considering only consecutive sample points along a view ray. We will subsequently call this incremental algorithm the *isosurface-first-crossing-probability* (IFCP) algorithm.

By introducing the negative no-crossing event $N_i^- := Y_1^- \cap Y_2^- \cap ... \cap Y_i^-$, we can now propose the following rule for updating $P(C_i^+)$ in interval I_i along a ray:

$$P(C_i^+) = P(N_i^-) \frac{P(Y_i^- \cap Y_{i+1}^+)}{P(Y_i^-)} \tag{12}$$

$$P(N_{i+1}^-) = P(N_i^-) \frac{P(Y_i^- \cap Y_{i+1}^-)}{P(Y_i^-)} \tag{13}$$

Here, $P(N_i^-)$ can be computed in-place and $P(N_1^-) = P(Y_1^-)$ applies. Keeping in mind that $P(Y_i^- \cap Y_{i+1}^+) = P(Y_i^-) - P(Y_i^- \cap Y_{i+1}^-)$, it is sufficient to compute the probabilities $P(Y_i^-)$ and $P(Y_i^- \cap Y_{i+1}^-)$ for each interval I_i. This is done using the SDF values ψ_i and ψ_{i+1}, the correlation ρ_i in interval I_i, as well as the univariate (Φ_1) and bivariate (Φ_2) standard normal cumulative distribution functions:

$$P(Y_i^-) = \Phi_1(-\psi_i) \tag{14}$$

$$P(Y_i^- \cap Y_{i+1}^-) = \Phi_2(-\psi_i, -\psi_{i+1}; \rho_i) \tag{15}$$

4.2. Probability Mapping

The isosurface first crossing probability p_i is then mapped to opacity according to the following considerations. In volume rendering an optical emission-absorption model for accumulating color and opacity information along each ray of sight is employed. The overall opacity along a single ray is written as $\alpha = 1 - \exp(-\lambda)$, where λ can be interpreted as the number of small opaque particles the ray hits on its way through the volume. For each ray through the volume an interactively specified maximum number of particles λ_{max} is distributed among the sample intervals I_i according to their probabilities p_i. This results in the local and global opacities:

$$\alpha(I_i) = 1 - \exp(-\lambda_{max} p_i) \tag{16}$$

$$\alpha\left(\bigcup_{i=1}^{n-1} I_i\right) = 1 - \exp\left(-\lambda_{max} \sum_{i=1}^{n-1} p_i\right), \tag{17}$$

where the global opacity represents the overall probability that the ray hits an isosurface along its way through the volume. While special attention has been put on the fact that only a linear relation between p_i and $\lambda_i = \lambda_{max} p_i$ is feasible. A linear relation between p_i and α_i is not possible as the probabilities are accumulated in an additive manner whereas opacities are updated multiplicatively along the ray.

4.3. Probability Types

An open question is whether the IFCP algorithm can also be applied when the ray hits two isosurfaces that have no stochastic dependence (e.g. because they are too far away from each other). Let us assume that the ray hits an isosurface with a significant probability (e.g. 0.5) in the sample interval $I = [\mathbf{s}_i, \mathbf{s}_{i+u}]$ and also in interval $J = [\mathbf{s}_j, \mathbf{s}_{j+v}]$ with $i + u \ll j$ and $\rho(Y(\mathbf{s}_{i+u}), Y(\mathbf{s}_j)) \approx 0$. The probabilities that are computed for all subintervals in J are *all* conditioned under the *same* assumption that there was no crossing in I. Thus, relative to each other, all sub-probabilities for J describe the positional variability in J. Furthermore, all values grow by the same factor if the true crossing probability for I approaches 0.

We will call the overall probabilities $\sum_{k=i}^{i+u-1} p_k$ and $\sum_{k=j}^{j+v-1} p_k$ for regions with low correlation between each other *probabilities of occurrence* (PO). The sub-probabilities within regions of high correlation (e.g. around the maximum likelihood position in I and respectively in J) will be called *probabilities of position* (PP). The IFCP algorithm has the nice property that while computing the PPs, it simultaneously combines the POs in the correct visibility order. It further guarantees that the overall crossing probability along the entire ray never exceeds 1.

Figure 2 illustrates the concept described above for two correlation assumptions. If independence is assumed ($\rho_i = 0$), the ray crosses the isosurface with much higher probability for the first time at an earlier stage compared to the assumption of maximum correlation. It can be seen clearly that the IFCP values for the second crossing are significantly lower if there is a high PO for the first crossing and vice versa. Secondly, the PPs for each crossing do almost not change. The illustration also reveals the importance of incorporating correlation information in the computation of probabilities for obtaining correct PP and PO values.

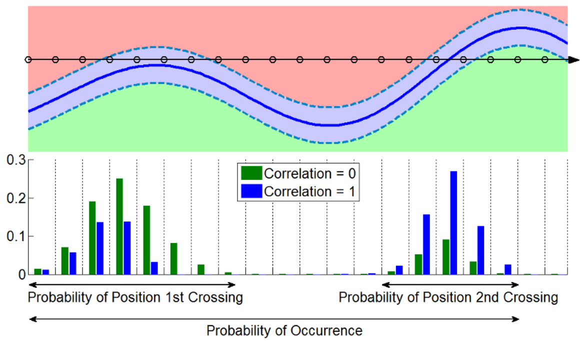

Figure 2: *The sampling along a ray (black) on a 2D slicing plane in a 3D dataset is shown. Negative values (red) are separated from positive values (green) by an 0-isosurface (blue). Its uncertainty is indicated by the blue area, representing the isosurface positions for up to $\pm\sigma$. The lower illustration shows the positive first crossing probabilities $P(C_i^+)$ as computed by our IFCP algorithm for each interval and under the assumption of zero (green) and maximum (blue) correlation between consecutive sample points.*

5. Geometric Variability

A major problem in visualizing isosurface variability is that the effectiveness of the visual perception of the variability depends on the viewing direction. If the uncertainty only reflects in the opacity variation, possible isosurface displacements, in general, can be only visualized if the viewing direction is nearly orthogonal to the surface normal. Similarly, since the SDF does not contain any information on the spatial distance variability, for a normal-parallel view the accumulation of colors that are mapped from SDF values cannot reveal the spatial isosurface variation in viewing direction.

Thus, a method is required that preserves the positional uncertainty information independently of the viewing direction. To achieve this, we propose a measure of the spatial isosurface variation due to the uncertainty. This measure is then used for assigning colors that emphasis the geometric surface variability.

5.1. SDF Surfaces

To reveal the uncertainty that is related to the shape of an isosurface, we incorporate shading effects into uncertainty volume rendering. Therefore, the vector pointing towards the direction of maximum increase in isosurface crossing probability is used. Except for the sign, this vector is equivalent to the gradient $\nabla\Psi_\theta(\mathbf{x}_i)$ of the stochastic distance function. Setting $t = \Psi_\theta(\mathbf{x}_i)$, this gradient is located orthogonal to the set

$$\vartheta_\theta(t) := \{\mathbf{x} \in \mathbb{S} : \Psi_\theta(\mathbf{x}) = t\}, \tag{18}$$

which contains all points having the same SDF value and, thus, the same stochastic distance from the isovalue. This set is commonly referred to as *SDF surface*.

SDF surface rendering is a common approach for visualizing positional isosurface uncertainty. For instance, in [ZWK10] $\vartheta_\theta(1)$ and $\vartheta_\theta(-1)$ were used to indicate the spatial region that contains the isosurface with a probability of 0.68. In our algorithm the gradient $\nabla\Psi_\theta$ is computed on-the-fly from the SDF values at the grid points, and it is then used for revealing the geometric variability of isosurfaces via shading effects and for estimating Euclidean distances between the mean surface and possible isosurface positions.

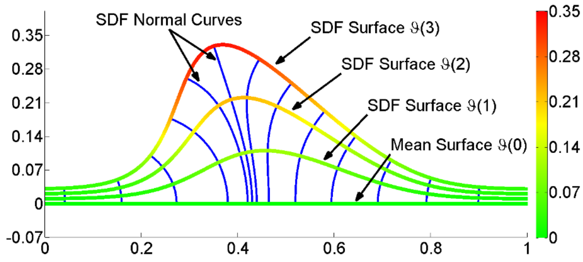

Figure 3: *This illustration shows the mean isosurface (green) of a 2D dataset, as well as three positive SDF surfaces. SDF normal curves (blue) are displayed for several points on the $\vartheta_\theta(3)$ surface. Points on the SDF surfaces are color coded with respect to the length of their normal curve to the intersection point with $\vartheta_\theta(0)$ - from green (small distance) to red (large distance). The magnitude of the numbers on the axes and on the color bar are related to Euclidean distances in the 2D domain.*

5.2. Spatial Distance Estimation

The positional uncertainty can be perceived in normal-orthogonal viewing direction because the opacity decreases with increasing spatial distance from the *mean surface* $\vartheta_\theta(0)$. This distance mainly varies orthogonal to the ray direction. In normal-parallel direction, however, the spatial distance varies in viewing direction, requiring to use an additional visual representation to show this variation.

To visually encode the spatial distance of a point on a SDF surface $\vartheta_\theta(t)$ to the mean surface $\vartheta_\theta(0)$, we first have to derive a measure that estimates this distance. Therefore, we define so called *SDF normal curves* $\gamma_\theta^x : \mathbb{R} \to \mathbb{S}$ for a point $\mathbf{x} \in \mathbb{S}$ using the following differential equation:

$$\frac{\mathrm{d}\gamma_\theta^x}{\mathrm{d}t}(t) = \nabla\Psi_\theta(\gamma_\theta^x(t)) \ , \ \gamma_\theta^x(0) = \mathbf{x} \tag{19}$$

Each normal curve crosses *all* SDF surfaces orthogonal. The magnitude of its derivative describes the amount of change in SDF value for an infinitesimal change in the spatial domain. The distance $d(\mathbf{x})$ of point $\mathbf{x} \in \vartheta_\theta(t)$ for $t \neq 0$ from the mean surface is now defined as the length of the normal curve γ_θ^x between $\mathbf{x}$ and its intersection point with $\vartheta_\theta(0)$ in 3D space (see Figure 3 for an illustration of this concept in 2D).

The "length" of the curve in SDF space is actually the SDF difference $|\Psi_\theta(\mathbf{x})|$ between $\vartheta_\theta(\mathbf{x})$ and $\vartheta_\theta(0)$. Thus, we obtain the equation

$$\int_0^{d(\mathbf{x})} \left\|\nabla\Psi_\theta(\gamma_\theta^x(t))\right\| \mathrm{d}t = |\Psi_\theta(\mathbf{x})| \,. \tag{20}$$

For simplicity we assume that $\|\nabla\Psi_\theta\|$ is constant along the considered curve segment, which means a linear increase/decrease in isosurface crossing probability along the SDF normal curve. Even though this assumption could be violated for large values of $|\Psi_\theta(\mathbf{x})|$, it should be quite reasonable for SDF surfaces close to the respective mean surface. Finally, the distance can be estimated as

$$d(\mathbf{x}) = \frac{|\Psi_\theta(\mathbf{x})|}{\|\nabla\Psi_\theta(\mathbf{x})\|}, \tag{21}$$

which provides a good indication of how strong a point $\mathbf{x}$ is deviated from the mean surface $\vartheta_\theta(0)$.

6. Visualization

For visualizing the positional and geometrical variability of a particular isosurface in an uncertain 3D scalar field, we use front-to-back volume ray-casting and compute the opacity according to the IFCP approach, in which the isovalue is interactively specified by the user using a slider. At each sample point $\mathbf{s}_i$, the spatial distance estimate $d(\mathbf{s}_i)$ is mapped to a HSV color value, with the distance being encoded into the *hue channel*. Based on a user-defined maximum distance d_{max}, the range $[0, d_{max}]$ is linearly mapped to the color map [green $\to$ yellow $\to$ red], and values greater than d_{max} are clamped to d_{max}. To integrate shading effects and, thus, to highlight the shape of the SDF surface, the cosine between the ray direction and the SDF gradient $\nabla\Psi_\theta$ is used to modulate the *value* of the HSV color sample. Here we allow a value reduction of at most 50%.

Color coding the spatial distance from the mean surface along the SDF normal curves allows for an intuitive perception of the isosurface variability in normal-parallel viewing direction. However, this approach has a drawback when the isosurface is cut by a slicing plane. In this case the color distribution is somewhat misleading since "color isocontours" do not necessarily represent a single SDF value. Therefore, on slicing planes a color scheme based on SDF related measures, e.g., as proposed in [PH10], gives a better impression of the spatial variability.

In order to overcome this limitation we use SDF isocontours on slicing planes, indicating its intersection with the SDF surfaces $\vartheta(0)$, $\vartheta(\pm 1)$, $\vartheta(\pm 2)$, etc. with a ± 0.1 tolerance. The SDF magnitude is coded into the blue channel using the LCP value introduced in [PH10]. As illustrated in Figure 4, this gives a clear impression of the relation between SDF values and spatial distances on slicing planes.

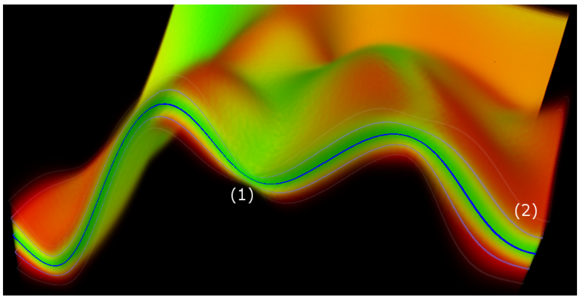

Figure 4: *An uncertain 3D signed distance field to a 2D topographic height map is shown. Multiple instances to a randomly displaced height map were generated, and the mean and standard deviations where computed from these instances. SDF isocontours on slicing planes indicate the set $\vartheta_\theta(0)$ (blue) and the sets $\vartheta_\theta(\pm i)$ with decreasing opacity and saturation. Note the relation between converging isocontours and low spatial distance (green) in (1) and between diverging contours and high spatial distance (red) in (2)*

In section 4.3 we have discussed the concept of probabilities of occasion and position. In order to integrate this concept into the visualization we desaturate areas with high PO but low correlation to the mean surface. For each sample point the spatial distance $d(\mathbf{s}_i)$ is used for computing a correlation coefficient in $\nabla\Psi_\theta$ direction using the ECF. This coefficient is linearly mapped to *saturation*. Thus, areas with a high spatial distance and a low correlation to values on the mean surface receive a lower saturation, indicating their independence and significance as PO area. In this way the user can visually differentiate between possible isosurface positions with high positional distribution on the one hand, and regions which might contain an isosurface but are stochastically independent from those PP areas on the other hand.

In addition, SDF surfaces can be rendered as add-on to the IFCP approach. A SDF value can be specified interactively by the user and the visualized surface can help to analyze stochastic geometrical and topological changes or to visually link stochastic and spatial distances. Further interaction mechanisms include the specification of the maximum opacity by controlling the respective number of particles λ_{max} (cf. 4.1) as well as the range $[0, d_{max}]$ of the spatial distance, which is mapped to the given color map.

7. Results and Analysis

To validate the effectiveness of the proposed uncertainty visualization techniques we have conducted experiments on uncertain 3D scalar fields given on tetrahedral grids. The following datasets were used:

- The GEO dataset was generated by seismic tomography, where recorded seismic waves were used for inferring structures in the earth's mantle below the Indo-Australian Plate. The scalar values represent the magnitudes of seismic wave velocities, enabling to separate subsurface structures with high and low velocities. As the computations were performed on incomplete and noisy data, the position of separating surfaces is highly affected by uncertainty [Käu10].
- The ATMOS dataset shows a 3D temperature field in the exosphere above Europe and the North Atlantic Ocean. It contains the mean values of multiple fields that were simulated by the European Centre for Medium-Range Weather Forecasts using different input parameters [Eur].

In Figure 1 (a) the GEO dataset is visualized using the IFCP algorithm (with distance dependent correlations incorporated) in combination with distance based coloring. In (b) the data is visualized using the same sampling distance along the view rays as in (a), but uncorrelated data samples were assumed ($\rho_i = 0$). Since the local data continuity and, thus, the stochastic dependency between nearby data samples was not considered, the isosurface crossing probabilities are strongly overestimated. This results in artificial bridging structures and a misleading probability visualization.

Figure 1 (d) shows a visualization of an uncertain isosurface in the ATMOS dataset using the IFCP algorithm. SDF values were linearly mapped to color. In (c) the same approach was used, but SDF values were mapped to color based on their spatial deviation from the mean surface along normal curves. By visualizing SDF isocontours on a slicing plane, the positional variability of the isosurface can be revealed locally in either case. Globally, and where the viewing direction is parallel to the normal of the isosurface, our approach (c) emphasizes the strength of the spatial deviation from the mean surface in convex *and* concave regions. Since SDF values do not contain any spatial distance information, the visualization in (d) fails in depicting the uncertainty with respect to the shape of the mean surface.

The potential of the proposed uncertainty visualization techniques for analyzing the effect of uncertainty on specific data features is demonstrated in Figure 5. In (a), the surface to a given isovalue is shown. In (b), the IFCP algorithm and spatial distance coloring were used under the assumption of homogeneous correlation ($\rho_i = 1$). The confidence volume containing the isosurface with a certain probability is enclosed by two stochastic distance surfaces in (c). The uncertainty visualization highlights the region where the simulated temperature field is rather sensitive to the input parameters of the simulation, indicating that the forecast for

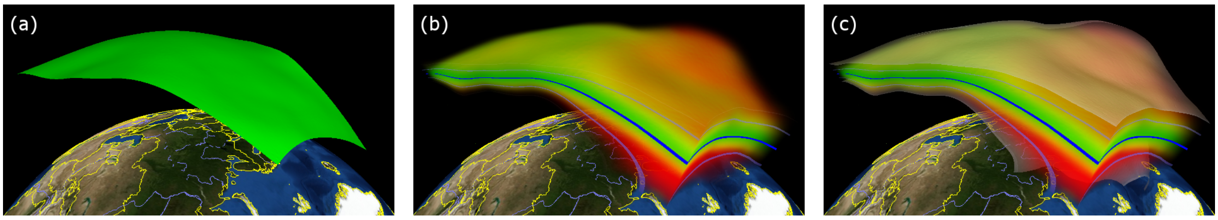

Figure 5: *(a) The mean surface for a temperature isovalue in the ATMOS dataset. (b) The IFCP algorithm in combination with distance dependent color mapping. (c) SDF surfaces $\vartheta(\pm 2)$ emphasize the uncertainty in isosurface shape.*

this region is not reliable. This information suggests to improve either on the physical forecast model, the used initial conditions, or the employed computational scheme to obtain a less sensitive and, thus, more reliable result.

An example which demonstrates the suitability of our approach for detecting possible topology changes due to uncertainty is shown in the visualization of the GEO dataset in Figure 6. In (a), the mean isosurface separating subsurface structures with high and low seismic wave velocities in the earth mantle below Australia is visualized. If the geometric variability of the separating surface due to uncertainty (constant correlation of $\rho_i = 1$) is visualized (b), additional "bridging" structures occur with a certain probability (1). Notably these structures and their geometrical appearance cannot be detected if uncertainty is ignored or only used to color the mean surface. To facilitate an improved assessment of the uncertainty related to the shape of an isosurface, and to employ the possibilities of a surface structure for integrating shading effects, the SDF surfaces $\vartheta(\pm 2)$ are incorporated into the visualization in (c).

In (d), with respect to (b) an anisotropic correlation decrease is assumed. The result is a significantly higher surface crossing probability along the view rays in area (2). In this example, saturation was chosen as an indication of high distance from the mean surface and low correlation. Thus, the specific color coding reveals high local stochastic independence rather than high local positional surface variability as major cause of the crossing probability in (2).

This information is important for analyzing the relationship between uncertainty parameters, like standard deviations and correlation structures. Especially in seismic tomography, high correlations are assigned to areas with high uncertainty for regularization purposes, and these correlations are then incorporated into a prior stochastic model. In this way areas with high PO concurrency, like in (d), can be avoided and uncertainty datasets obtained, clearly showing the positional variability like in (b). The visual analysis of the effect of such prior stochastic models is of great importance for steering the tomography process towards reduced uncertainty. The visual integration of the PO/PP concept, as discussed in 4.3, is another new strong benefit of our proposed methods, since it enables differentiating between regions with high correlation and, therefore, high positional uncertainty, and areas with high stochastic independence and, therefore, high occurrence uncertainty.

8. Implementation and Performance Details

All of our results were rendered into a 1K $\times$ 768 viewport using volume ray-casting on the GPU as proposed in [Wei05]. Tetrahedral elements — represented by four indices to their vertices — were stored in an element buffer. Each element was accompanied by a correlation tensor and four additional links to their neighboring elements. Shared vertex buffers were used to store the vertex coordinates as well as the mean values and standard deviations. View rays were traversed with a given sampling distance by subsequently computing ray-cell intersections and following the respective link to the next element. Barycentric interpolation was used to reconstruct a continuous field, and early-ray termination was performed at an optical attenuation above 0.95.

When executing the IFCP algorithm, the update operations (12) are performed at every sample interval along the view rays. This requires evaluating and interpolating per-vertex SDF values, and evaluating the probabilities $P(Y_i^-)$ and $P(Y_i^- \cap Y_{i+1}^-)$ as stated in (14). To reduce the computations required for evaluating the distribution functions Φ_1 and Φ_2, and to avoid precision problems caused by real number divisions in (12), function values $\Phi[a,b,\rho] = \Phi_2(a,b;\rho)/\Phi_1(a)$ were pre-computed, e.g., as described in [AS64, DW90], and stored in a 256^3 texture map with $a,b \in [-5.08, 5.08]$ and $\rho \in [0,1]$. This texture map is used at runtime as a lookup table, resulting in an approximation error below floating point precision.

On our target architecture, a 2.83 GHz Core 2 Quad processor equipped with a NVIDIA Quadro FX5800, the IFCP algorithm roughly doubles the visualization time per frame compared to isosurface ray-casting. For instance, the visualization of the isosurface in the GEO dataset (3.3 million tetrahedral elements) shown in Figure 6 (a) requires 85 milliseconds (ms), while the IFCP algorithm takes about 150 ms. 80 MBytes are required to store the mean values, the standard deviations, and the correlation tensors, plus additional 65 MBytes consumed by the pre-computed 3D look-up table. The loss of performance in the IFCP algorithm is

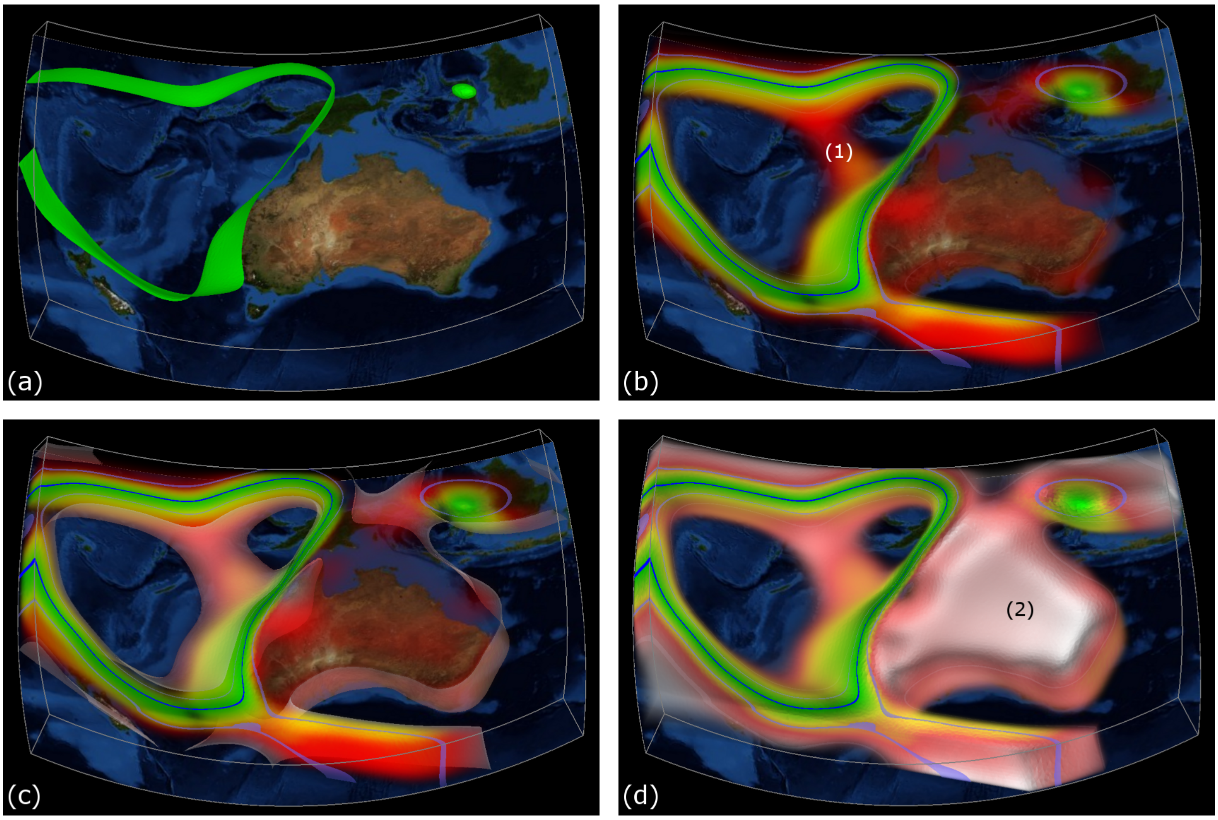

Figure 6: *(a) A separating isosurface in a seismic tomography dataset is shown. (b) The IFCP algorithm in combination with distance dependent color mapping (homogeneous correlation of $\rho_i = 1$) reveals a possible topological link in (1). (c) SDF surfaces $\vartheta(\pm 2)$ emphasis the isosurface uncertainty with respect to shape. (d) An anisotropic correlation decrease is assumed. Compared to (b), higher crossing probabilities are determined in (2), but correlation based saturation reveals high stochastic independence rather than high local positional isosurface variability as major cause.*

mainly due to the enlarged memory footprint for computing and interpolating SDF values and gradients on the fly, and for accessing the pre-computed distribution functions.

9. Conclusion

We have presented a novel approach for computing reliable probabilities of position and occurrence for isosurface crossings in uncertain 3D scalar fields. We have achieved this by incorporating distance dependent correlations into our approach. An efficient update-scheme allows integrating the proposed algorithm into front-to-back ray-casting. A new measure for estimating the distance between possible isosurface variations and the mean surface has been developed. This measure is used as input for a color mapping scheme, which allows for an effective visualization of isosurface variability independent of the viewing direction. We have demonstrated that our approach results in an intuitive understanding of the effect of uncertainty on isosurfaces in 3D scalar fields.

In the future, we will pursue further research to provide deeper insights into 3D correlation structures and to investigate the sensitivity of the probability to these structures. We will also analyze the approximation error that is inherent to the proposed computation of the spatial distance measure, and we will investigate the effect of this error on the visualization. Finally, we will consider the integration of sample based probability distributions, like in Monte Carlo simulations, and multimodal density models into our approach.

Acknowledgments

We would like to thank the European Centre for Medium-Range Weather Forecasts for providing the ATMOS dataset, and Paul Käufl from the Geophysics Group at LMU München for providing the GEO dataset. The work was funded by the Munich Centre for Advanced Computing and the International Graduate School of Science and Engineering (IGSSE) at the Technische Universität München.

References

[AS64] ABRAMOWITZ M., STEGUN I.: *Handbook of mathematical functions with formulas, graphs, and mathematical tables*. Dover publications, 1964. 8

[BAF08] BOSTROM A., ANSELIN L., FARRIS J.: Visualizing Seismic Risk and Uncertainty. *Annals of the New York Academy of Sciences 1128*, 1 (2008), 29–40. 2

[Bro04] BROWN R.: Animated visual vibrations as an uncertainty visualisation technique. In *GRAPHITE* (2004), ACM, pp. 84–89. 2

[DKLP02] DJURCILOV S., KIM K., LERMUSIAUX P., PANG A.: Visualizing scalar volumetric data with uncertainty. *Computers & Graphics 26*, 2 (2002), 239–248. 2

[DMJRM00] DE MAESSCHALCK R., JOUAN-RIMBAUD D., MASSART D.: The mahalanobis distance. *Chemometrics and Intelligent Laboratory Systems 50*, 1 (2000), 1–18. 3

[DW90] DREZNER Z., WESOLOWSKY G.: On the computation of the bivariate normal integral. *Journal of Statistical Computation and Simulation 35*, 1 (1990), 101–107. 8

[Eur] EUROPEAN CENTRE FOR MEDIUM-RANGE WEATHER FORECASTS: Demeter temperature ensemble. Available online at http://www.ecmwf.int. 7

[GR04] GRIGORYAN G., RHEINGANS P.: Point-based probabilistic surfaces to show surface uncertainty. *Visualization and Computer Graphics, IEEE Transactions on 10*, 5 (2004), 564–573. 2

[GS06] GRIETHE H., SCHUMANN H.: The visualization of uncertain data: Methods and problems. In *Proceedings of SimVis 2006* (2006), pp. 143–156. 2

[Joh04] JOHNSON C.: Top scientific visualization research problems. *Computer graphics and applications, IEEE 24*, 4 (2004), 13–17. 1

[JS03] JOHNSON C., SANDERSON A.: A next step: Visualizing errors and uncertainty. *Computer Graphics and Applications, IEEE 23*, 5 (2003), 6–10. 2

[Käu10] KÄUFL P.: *Object-based Probabilistic Full Waveform Tomography*. Master's thesis, Geophysics, LMU München, 2010. 7

[KVUS*05] KNISS J., VAN UITERT R., STEPHENS A., LI G., TASDIZEN T., HANSEN C.: Statistically quantitative volume visualization. 2

[KWTM03] KINDLMANN G., WHITAKER R., TASDIZEN T., MOLLER T.: Curvature-based transfer functions for direct volume rendering: Methods and applications. In *Visualization, 2003. VIS 2003. IEEE* (2003), IEEE, pp. 513–520. 2

[LFLH07] LI H., FU C., LI Y., HANSON A.: Visualizing large-scale uncertainty in astrophysical data. *Visualization and Computer Graphics, IEEE Transactions on 13*, 6 (2007), 1640–1647. 2

[LLPY07] LUNDSTROM C., LJUNG P., PERSSON A., YNNERMAN A.: Uncertainty visualization in medical volume rendering using probabilistic animation. *Visualization and Computer Graphics, IEEE Transactions on 13*, 6 (2007), 1648–1655. 2

[Mah36] MAHALANOBIS P.: On the generalized distance in statistics. In *Proceedings of the National Institute of Science, Calcutta* (1936), vol. 12, p. 49. 3

[MRH*05] MACEACHREN A., ROBINSON A., HOPPER S., GARDNER S., MURRAY R., GAHEGAN M., HETZLER E.: Visualizing Geospatial Information Uncertainty: What We Know and What We Need to Know. *Cartography and Geographic Information Science 32*, 3 (2005), 139–161. 2

[OGHT10] OTTO M., GERMER T., HEGE H., THEISEL H.: Uncertain 2d vector field topology. In *Computer Graphics Forum* (2010), vol. 29, Wiley Online Library, pp. 347–356. 2

[PH10] PÖTHKOW K., HEGE H.-C.: Positional uncertainty of isocontours: Condition analysis and probabilistic measures. *IEEE Transactions on Visualization and Computer Graphics 99*, PrePrints (2010). 1, 2, 3, 7

[PWL97] PANG A., WITTENBRINK C., LODHA S.: Approaches to uncertainty visualization. *The Visual Computer 13*, 8 (1997), 370–390. 2

[RLBS03] RHODES P., LARAMEE R., BERGERON R., SPARR T.: Uncertainty visualization methods in isosurface rendering. In *Eurographics* (2003), Citeseer, pp. 83–88. 2

[RN88] RODGERS J., NICEWANDER W.: Thirteen ways to look at the correlation coefficient. *American Statistician 42*, 1 (1988), 59–66. 3

[SZD*10] SANYAL J., ZHANG S., DYER J., MERCER A., AMBURN P., MOORHEAD R.: Noodles: A Tool for Visualization of Numerical Weather Model Ensemble Uncertainty. *IEEE Transactions on Visualization and Computer Graphics* (2010). 2

[Tar05] TARANTOLA A.: *Inverse problem theory and methods for model parameter estimation*. Society for Industrial Mathematics, 2005. 3

[THM*05] THOMSON J., HETZLER E., MACEACHREN A., GAHEGAN M., PAVEL M.: A typology for visualizing uncertainty. In *Proc. SPIE* (2005), vol. 5669, Citeseer, pp. 146–157. 2

[Wei05] WEILER M.: *Hardware-beschleunigte Volumenvisualisierung auf adaptiven Datenstrukturen*. PhD thesis, Universitätsbibliothek der Universität Stuttgart, 2005. 8

[WPL02] WITTENBRINK C., PANG A., LODHA S.: Glyphs for visualizing uncertainty in vector fields. *Visualization and Computer Graphics, IEEE Transactions on 2*, 3 (2002), 266–279. 2

[ZWK10] ZEHNER B., WATANABE N., KOLDITZ O.: Visualization of gridded scalar data with uncertainty in geosciences. *Computers & Geosciences* (2010). 2, 3, 6